Ultrasensitive magnetic field sensor based on an in-fiber Mach–Zehnder interferometer with a magnetic fluid component

Zhengyong Li,[1] Changrui Liao,[1,3] Jun Song,[1] Ying Wang,[1] Feng Zhu,[1] Yiping Wang,[1,*] and Xiaopeng Dong[2]

[1]*Key Laboratory of Optoelectronic Devices and Systems of Ministry of Education and Guangdong Province,*
College of Optoelectronic Engineering, Shenzhen University, Shenzhen 518060, China
[2]*School of Information Science and Engineering, Xiamen University, Xiamen 361005, China*
[3]*e-mail: cliao@szu.edu.cn*
Corresponding author: ypwang@szu.edu.cn

An ultrasensitive magnetic field sensor based on a compact in-fiber Mach–Zehnder interferometer (MZI) created in twin-core fiber (TCF) is proposed, and its performance is experimentally demonstrated. A section of TCF was spliced between two sections of standard single-mode fibers, and then a microchannel was drilled through one core of the TCF by means of femtosecond laser micromachining. The TCF with one microchannel was then immersed in a water-based Fe_3O_4 magnetic fluid (MF), forming a direct component of the light propagation path, and then sealed in a capillary tube, achieving a magnetic sensing element, which merges the advantages of an MZI with an MF. Experiments were conducted to investigate the magnetic response of the proposed sensor. The developed magnetic field sensor exhibits a linear response within a measurement range from 5 to 9.5 mT and an ultrahigh sensitivity of 20.8 nm/mT, which, to our best knowledge, is 2 orders of magnitude greater than other previously reported magnetic sensors. The proposed sensor is expected to offer significant potential for detecting weak magnetic fields.   © 2016 Chinese Laser Press

OCIS codes: (260.3160) Interference; (060.4005) Microstructured fibers; (060.2370) Fiber optics sensors.
http://dx.doi.org/10.1364/PRJ.4.000197

1. INTRODUCTION

Recently, magnetic field sensors have been widely investigated for applications in various fields such as aerospace, intelligent weapons, aviation, and controlled nuclear fusion [1]. Optical fiber sensors play an important role in magnetic field detection because of their advantages of small size, high sensitivity, short response time, and anti-electromagnetic interference [2–4]. Magnetic fluid (MF) is a kind of novel functional material that has many remarkable magneto-optical properties such as tunable refractive index (RI), Faraday effect, and birefringence effect [5,6]. These unique properties have been employed in numerous optical fiber sensors incorporating MFs such as fiber Bragg gratings [7,8], modal interferometers [9–11], photonic crystal fibers [12], and Fabry–Perot and Michelson [13] interferometers. The core-offset microfiber configuration is low cost and easy to fabricate, but it employs intensity demodulation that cannot ignore the power fluctuation of the optical source [1]. The single-mode fiber (SMF)–multimode fiber–SMF and the nonadiabatic fiber taper configurations demonstrate the magnetic field sensitivities of 0.905 and –0.077 nm/mT, respectively [10,14]. However, these sensors are based on the interaction between the weak evanescent field and an external MF that limits their sensitivity to magnetic field.

To overcome these issues, we present a Mach–Zehnder interferometer (MZI) combined with MF in twin-core fiber (TCF) for ultrasensitive magnetic field measurement. The sensor is fabricated by splicing a short section of

TCF between two SMFs and then drilling a microchannel through one core of TCF by use of a femtosecond laser. The microchannel is then filled with MF and the TCF region is sealed by a capillary tube. Based on the tunable RI property of MF, the RI difference between the medium and the pristine core will be changed with the variation of external magnetic field. This sensor exhibits an ultrahigh magnetic field sensitivity of 20.8 nm/mT from 5 to 9.5 mT, which, to the best of our knowledge, is the highest sensitivity among the reported magnetic field sensors and might be used for weak magnetic field detection.

2. OPERATING PRINCIPLE AND FABRICATION

The schematic diagram of the proposed magnetic field sensor is illustrated in Fig. 1. The sensor is made up of a short section of TCF being spliced between two SMFs, SMF_1 and SMF_2. The two splicing joints operate as optical splitter and combiner, respectively. The light propagating along SMF_1 is equally coupled to two cores of TCF at the left splicing joint. However, the light propagating through the micromachined core will be uniquely affected by the interposed medium, which induces a phase shift relative to light propagating along the pristine core. The shape of the two TCF cores is an asymmetric ellipse, and the TCF length is ∼200 μm so that the light cross talk between the two cores can be negligible. Light propagation through the two cores can be reasonably
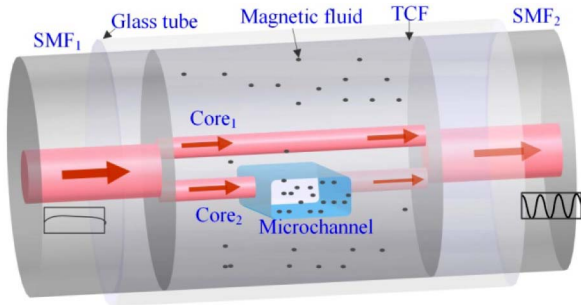
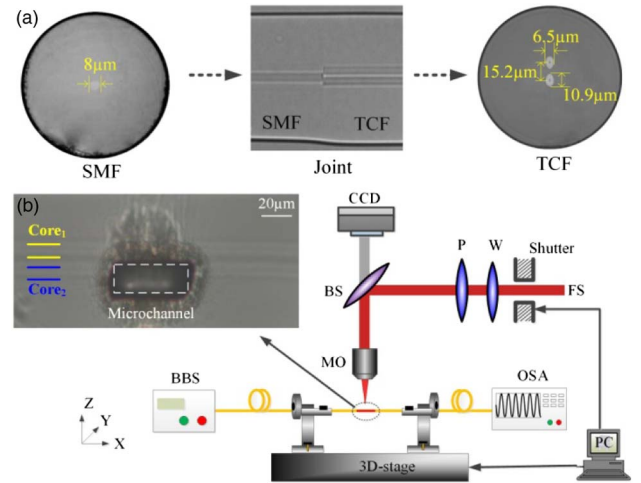Fig. 1.   Schematic diagram of the proposed magnetic field sensor.

Fig. 2.   (a) Optical microscope image of the cross-sectional morphology of SMF and TCF, including the dimensions of the elliptical TCF cores and the splicing point between SMF_1 and TCF. (b) Schematic diagram of the femtosecond laser micromachining system. The insert image shows an optical microscope image of the drilled microchannel through $Core_2$.

assumed to be independent. Finally, two output beams are recoupled into SMF_2 at the right splicing joint.

When two output beams, I_{core1} and I_{core2}, propagating through their respective cores of the TCF are recombined in SMF_2, the phase difference between the two output beams results in interference. The interference intensity of the MZI can be expressed as

$$I = I_{core1} + I_{core2} + 2\sqrt{I_{core1}I_{core2}}\cos\left(\frac{2\pi L \Delta n}{\lambda} + \varphi_0\right), \quad (1)$$

where λ is the wavelength; L is the length of the microchannel with respect to the propagation path; $\Delta n = n_{core} - n_{channel}$ is the effective RI difference between the two interference arms, where n_{core} and $n_{channel}$ are the effective RI of the core and the medium in the microchannel; and φ_0 is the initial phase of the interferometer. According to Eq. (1), the output intensity attains the minimum value under the following conditions:

$$\lambda_m = \frac{2\pi L \Delta n}{(2m+1)\pi}, \quad (2)$$

where m is an integer and λ_m is the wavelength of the mth order fringe dip. Here, the fringe means the interference spectrum. The free spectral range (FSR) of the fiber interferometer can be expressed as

$$FSR = \frac{\lambda^2}{\Delta n L}. \quad (3)$$

When the effective RI of the medium in the microchannel is changed, Δn will be changed and the mth attenuation dip will be shifted by the amount $\delta\lambda$, estimated as

$$\delta\lambda \approx \frac{2L(\Delta n + \delta n)}{2m+1} - \frac{2L\Delta n}{2m+1} = \frac{2L\delta n}{2m+1}. \quad (4)$$

The RI of MF is a function of the magnitude of the surrounding magnetic field. The spectrum of MF-based MZI will also be changed with variation of the surrounding magnetic field.

In this configuration, the SMF is Corning SMF-28 with core/cladding diameter of 8/125 μm, and TCF is supplied by Prof. Dong's group in Xiamen University. Figure 2(a) shows the cross section of two fibers and the morphology of the splicing joint. Here, the cladding diameter of TCF is 125 μm and the length of major/minor axes of the two elliptical cores are ~10.9 and ~6.5 μm, respectively. The sensor fabrication involves two steps. First, the left end of TCF is spliced with

SMF_1 by use of a commercial fusion splicer (Fujikura FSM-60s). To guarantee equal light intensity sent into the two cores, the offset distance between SMF_1 and TCF should be carefully adjusted by comparing the light intensity of the two cores of TCF when a red laser beam is launched into SMF_1. Next, the TCF is cut off with a remaining length of ~200 μm; then the right end of TCF is spliced with SMF_2 by an optimized offset value to obtain a maximum fringe visibility.

Second, a femtosecond laser (Spectra-Physics Solstice, 120 fs, 800 nm, 1 kHz, 4 mJ) is employed to drill the microchannel through the cladding and $Core_2$ of TCF. A schematic diagram of the femtosecond laser micromachining system is shown in Fig. 2(b). The laser beam passes through an attenuator made up of a half-wave plate (W) and polarizer (P) for adjusting the laser power in the range from 0 to 4 mJ, is reflected by the beam splitter (BS), and is then focused onto the fiber by an objective lens (MO) with an NA value of 0.25. The average power of pulses prior to the MO is maintained at ~20 mW. The CCD camera allows for real-time monitoring of the micromachining process. The fiber is fixed in parallel with the x axis of a computer-controlled 3D translation stage with a resolution of 10 nm. Fabrication of the microchannel is similar to that employed in a previously published procedure [15]. The microchannel is cleaned using alcohol after laser fabrication, and the completed microchannel is shown by the optical microscope image presented in Fig. 2(b). The relatively large surface roughness implies that the employed laser power was somewhat high. However, the processing parameters, including laser power and scanning speed, can be further optimized to obtain better surface quality.

The MF employed in this study consisted of Fe_3O_4 magnetic particles with an average diameter around 10 nm dispersed in water. The TCF-based MZI configuration is inserted within a section of capillary tube having an interior diameter of 250 μm. The MF is injected through one port of the glass tube, and glue is applied to seal the device. Due to capillary action, the microchannel becomes fully filled with MF.

Li *et al.*

Vol. 4, No. 5 / October 2016 / Photon. Res.   199

3. EXPERIMENTS AND RESULTS

The transmission spectra were measured during the overall fabrication process using a broadband light source (BBS) ranging from 1250 to 1650 nm and an optical spectrum analyzer (OSA) with a resolution of 0.05 nm, as indicated in Fig. 2(b). The black curve in Fig. 3 shows the transmission spectrum after splicing both SMFs with TCF, which indicates an absence of interference between light propagating through the separate cores. The two splicing joints between the SMFs and TCF cause an insertion loss of ~2.8 dB, whereas the cross talk between the two TCF cores is ignored, as discussed previously. The blue curve in Fig. 3 shows the transmission spectrum after completion of microchannel fabrication. Around 1563 nm, the fringe visibility and FSR are measured as ~4 dB and ~94 nm and the insertion loss is increased up to ~11 dB. Three factors may be responsible for this large insertion loss: (1) rough surface of the microchannel; (2) propagation loss of the unguided mode through the microchannel; and (3) connection loss at two splicing joints. By optimizing the machining parameters in fusion splicing and femtosecond laser micromachining, the insertion loss may be decreased to some degree. When the microchannel is filled with MF, there is only one fringe dip over the entire investigated wavelength range, as shown by the red curve of Fig. 3. According to Eq. (3), when the medium in the microchannel is changed to MF from air, the Δn between the $Core_1$ and MF will be sharply decreased, leading to the FSR being substantially increased so that only one fringe dip can be seen within the measured wavelength range.

A schematic diagram of the magnetic field sensing is demonstrated in Fig. 4, where the magnetic field generator is formed by two electromagnets and a Gauss meter is employed for reference. The MF-filled fiber magnetic field sensor is placed parallel between the two electromagnets, and a BBS and an OSA are connected with the sensor to measure its transmission spectrum in real time. The magnetic field is given by the magnetic field generator with a stability of ±0.01 mT, which is increased from 0 to 36 mT in 2 mT intervals. The temperature is maintained at 25°C in this experiment.

The dependence of the wavelength of fringe dip on the magnitude of magnetic field for an MF-filled magnetic field sensor employing a microchannel with $L = 55$ μm is presented in Fig. 5. It can be found that the fringe dip is nonlinearly shifted toward the longer wavelength with an increase of applied

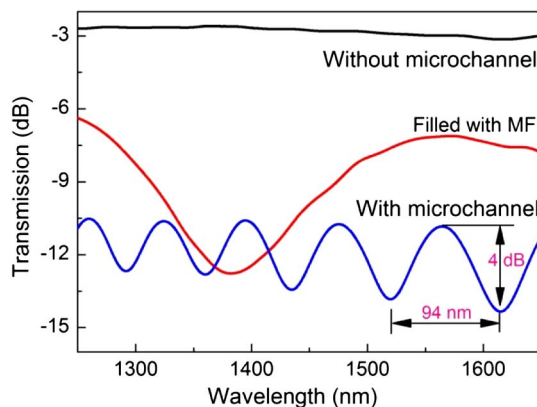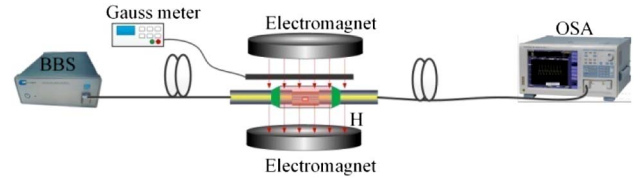Fig. 4.   Schematic diagram of magnetic field response measurement.

magnetic field. According to response sensitivity, its performance can be divided into four ranges, sluggish area (0–2 mT), high-sensitive area (2–12 mT), low-sensitive area (12–30 mT), and saturated area (>30 mT).

The RI of MF (n_{MF}) can be expressed via the expression $n_{MF} = \sqrt{\mu_r \cdot \varepsilon_{MF}}$, where μ_r and ε_{MF} are relative magnetic permeability and dielectric constant, respectively. When the MF is exposed to an external magnetic field, the ferromagnetic particles in the MF agglomerate and increasingly form magnetic columns, leading to phase separation and a resulting variation in the effective dielectric constant. As a result, the value of n_{MF} is altered. The effective dielectric constant ε_{MF} is expressed as

$$\varepsilon_{MF} = -\varepsilon_{col} - \varepsilon_{liq} + \frac{\sqrt{[\varepsilon_{col}(1-f) + \varepsilon_{liq}(f-1)]^2 + 4(1+f)^2 \varepsilon_{col}\varepsilon_{liq}}}{2(1+f)},$$

(5)

where ε_{col} represents the dielectric constant of a magnetic column, which is a constant; ε_{liq} is the dielectric constant of the liquid phase, which varies according to the magnitude of the magnetic field; and $f = (A_{col}/A)/(1 - A_{col}/A)$, where A_{col}/A represents the ratio of the area occupied by the magnetic columns to the total area, which is dependent on the magnitude of the external magnetic field. Hence, the ε_{MF} can affect the n_{MF}. The magnetic permeability $\mu_r = 1 + \chi$, where χ is the magnetic susceptibility depending on the magnitude of the magnetic field. The experimental result reveals that the value of n_{MF} depends on the magnitude of the magnetic field, which affects the value of Δn, leading to a significant dip shift.

Studies have shown that the relationship between n_{MF} and applied magnetic field is an S-type curve [14]. Because the

Fig. 3.   Transmission spectra of the pristine TCF and TCF with a microchannel filled with either air or an MF.
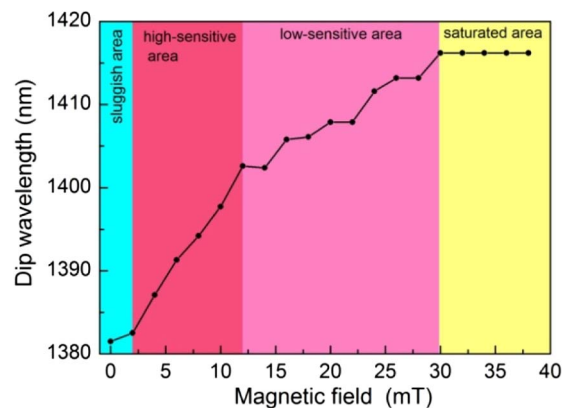

Fig. 5.   Variation of the fringe dip wavelength with respect to an applied magnetic field, divided into sluggish area, high-sensitive area, low-sensitive area, and saturated area.
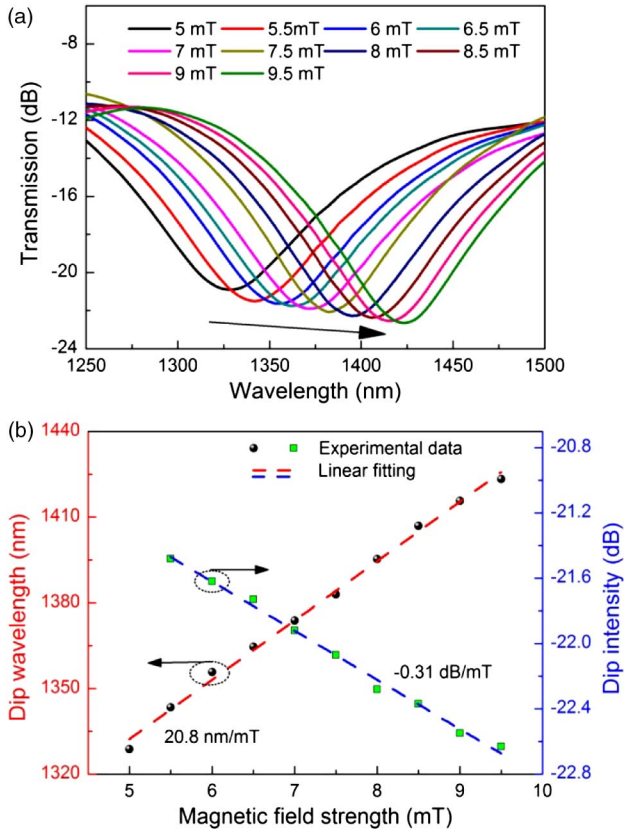
Fig. 6. (a) Transmission spectral evolution with an increasing applied magnetic field in the linear response region from 5 to 9.5 mT. (b) Variation of the fringe dip wavelength and dip intensity with respect to an applied magnetic field.

Fe_3O_4 magnetic particles are dispersed in water with a reckonable concentration and the initial magnetization, the value of n_{MF} changes little until the magnetic field exceeds the first critical point. When the magnetic field is further increased above the second critical point, the MF will become saturated, where the value of n_{MF} is hardly changed.

Another TCF-based MZI with the microchannel length of ~55 μm was fabricated to investigate its response over the linear range. The applied magnetic field was increased from 5 to 9.5 mT in intervals of 0.5 mT. The evolution of the transmission spectrum of the fiber magnetic field sensor as a function of magnetic field strength is presented in Fig. 6(a). The fringe dip is shifted to a longer wavelength with an increase of magnetic field strength. The relationship between dip wavelength and dip intensity and magnetic field strength are given in Fig. 6(b). They have good linear response for both cases with slopes of 20.8 nm/mT and −0.31 dB/mT.

The performance of other magnetic field sensors is compared with that of the proposed TCF-based MZI sensor, and the data is presented in Table 1. It can be seen that the magnetic field sensitivity of the TCF-based MZI sensor is by far the greatest among all sensors considered and was in some cases 2 orders of magnitude greater. In contrast to the structures of the other sensors, the TCF-based MZI employs an open MF-filled microchannel in which light can directly interact with MF in one of the interference arms of the MZI, which guarantees an ultrahigh magnetic field sensitivity.

Table 1. Comparisons of the Proposed TCF-Based MZI with Other Magnetic Field Sensors

Structure	Range (mT)	Wavelength Sensitivity (nm/mT)
Single-mode–multimode–single-mode [10]	0–22	0.905
Asymmetric optical fiber taper [16]	0–21.4	−0.16206
Taper-like and lateral-offset fusion splicing [9]	3.8–47.5	0.141
Michelson interferometer [13]	0–107	0.0649
Fabry–Perot interferometer [6]	0–40	0.431
Proposed MZI	5–9.5	20.8

4. CONCLUSION

We have experimentally demonstrated an ultracompact TCF-based MZI for magnetic field measurement with extremely high sensitivity. The two cores of the TCF are employed as the two interference arms of the MZI, and an open microchannel was fabricated in one of the cores by means of femtosecond laser micromachining in which MF was filled, forming a direct component of the light propagation path. The resulting magnetic field sensor exhibits an ultrahigh sensitivity of 20.8 nm/mT with a range from 5.0 to 9.5 mT, which, to the best of our knowledge, is the highest sensitivity compared with all other reported magnetic field sensors. This sensor might be used in weak magnetic field detection.

REFERENCES

1. J. Wu, Y. Miao, W. Lin, K. Zhang, B. Song, H. Zhang, B. Liu, and J. Yao, "Dual-direction magnetic field sensor based on core-offset microfiber and ferrofluid," IEEE Photon. Technol. Lett. **26**, 1581–1584 (2014).
2. Z. Li, Y. Wang, C. Liao, S. Liu, J. Zhou, X. Zhong, Y. Liu, K. Yang, Q. Wang, and G. Yin, "Temperature-insensitive refractive index sensor based on in-fiber Michelson interferometer," Sens. Actuators B **199**, 31–35 (2014).
3. Y. Wang, "Review of long period fiber gratings written by CO_2 laser," J. Appl. Phys. **108**, 081101 (2010).
4. Y. P. Wang, J. P. Chen, and Y. J. Rao, "Torsion characteristics of long-period fiber gratings induced by high-frequency CO_2 laser pulses," J. Opt. Soc. Am. B **22**, 1167–1172 (2005).
5. R. Gao, Y. Jiang, and S. Abdelaziz, "All-fiber magnetic field sensors based on magnetic fluid-filled photonic crystal fibers," Opt. Lett. **38**, 1539–1541 (2013).
6. S. Y. Yang, J. J. Chieh, H. E. Horng, C. Y. Hong, and H. C. Yang, "Origin and applications of magnetically tunable refractive index of magnetic fluid films," Appl. Phys. Lett. **84**, 5204–5206 (2004).
7. J. Zheng, X. Dong, P. Zu, L.-Y. Shao, C. C. Chan, Y. Cui, and P. P. Shum, "Magnetic field sensor using tilted fiber grating interacting with magnetic fluid," Opt. Express **21**, 17863–17868 (2013).
8. Y. Dai, M. Yang, G. Xu, and Y. Yuan, "Magnetic field sensor based on fiber Bragg grating with a spiral microgroove ablated by femtosecond laser," Opt. Express **21**, 17386–17391 (2013).

9. S. Dong, S. Pu, and H. Wang, "Magnetic field sensing based on magnetic-fluid-clad fiber-optic structure with taper-like and lateral-offset fusion splicing," Opt. Express **22**, 19108–19116 (2014).

10. Y. Chen, Q. Han, T. Liu, X. Lan, and H. Xiao, "Optical fiber magnetic field sensor based on single-mode-multimode-single-mode structure and magnetic fluid," Opt. Lett. **38**, 3999–4001 (2013).

11. J. Wu, Y. Miao, B. Song, W. Lin, H. Zhang, K. Zhang, B. Liu, and J. Yao, "Low temperature sensitive intensity-interrogated magnetic field sensor based on modal interference in thin-core fiber and magnetic fluid," Appl. Phys. Lett. **104**, 252402 (2014).

12. P. Zu, C. C. Chan, W. S. Lew, L. Hu, Y. Jin, H. F. Liew, L. H. Chen, W. C. Wong, and X. Dong, "Temperature-insensitive magnetic field sensor based on nanoparticle magnetic fluid and photonic crystal fiber," IEEE Photon. J. **4**, 491–498 (2012).

13. M. Deng, X. Sun, M. Han, and D. Li, "Compact magnetic-field sensor based on optical microfiber Michelson interferometer and Fe_3O_4 nanofluid," Appl. Opt. **52**, 734–741 (2013).

14. C. Y. Hong, S. Y. Yang, and H. C. Yang, "Control parameters for the tunable refractive index of magnetic fluid films," J. Appl. Phys. **94**, 3849–3853 (2003).

15. Y. Wang, M. Yang, D. N. Wang, S. Liu, and P. Lu, "Fiber in-line Mach–Zehnder interferometer fabricated by femtosecond laser micromachining for refractive index measurement with high sensitivity," J. Opt. Soc. Am. B **27**, 370–374 (2010).

16. M. Deng, D. Liu, and D. Li, "Magnetic field sensor based on asymmetric optical fiber taper and magnetic fluid," Sens. Actuators A **211**, 55–59 (2014).